remote sensing

MDPI

Article

A Synthetic Aperture Radar-Based Robust Satellite Technique (RST) for Timely Mapping of Floods

Meriam Lahsaini [1], Felice Albano [2], Raffaele Albano [3], Arianna Mazzariello [3] and Teodosio Lacava [2,*]

[1] Institute of Geosciences and Earth Resources (IGG), National Research Council (CNR), Via Moruzzi 1, 56126 Pisa, Italy; meriam.lahsaini@usmba.ac.ma
[2] Institute of Methodologies for Environmental Monitoring (IMAA), National Research Council (CNR), C.da Santa Loja, 85050 Tito Scalo, Italy; felice.albano12@gmail.com
[3] School of Engineering, University of Basilicata, 85100 Potenza, Italy; raffaele.albano@unibas.it (R.A.); arianna.mazzariello@unibas.it (A.M.)
* Correspondence: teodosio.lacava@cnr.it; Tel.: +39-097142724

Abstract: Satellite data have been widely utilized for flood detection and mapping tasks, and in recent years, there has been a growing interest in using Synthetic Aperture Radar (SAR) data due to the increased availability of recent missions with enhanced temporal resolution. This capability, when combined with the inherent advantages of SAR technology over optical sensors, such as spatial resolution and independence from weather conditions, allows for timely and accurate information on flood event dynamics. In this study, we present an innovative automated approach, SAR-RST-FLOOD, for mapping flooded areas using SAR data. Based on a multi-temporal analysis of Sentinel 1 data, such an approach would allow for robust and automatic identification of flooded areas. To assess its reliability and accuracy, we analyzed five case studies in areas where floods caused significant damage. Performance metrics, such as overall (OA), user (UA), and producer (PA) accuracy, as well as the Kappa index (K), were used to evaluate the methodology by considering several reference flood maps. The results demonstrate a user accuracy exceeding 0.78 for each test map when compared to the observed flood data. Additionally, the overall accuracy values surpassed 0.96, and the kappa index values exceeded 0.78 when compared to the mapping processes from observed data or other reference datasets from the Copernicus Emergency Management System. Considering these results and the fact that the proposed approach has been implemented within the Google Earth Engine framework, its potential for global-scale applications is evident.

Keywords: Sentinel 1; SAR-RST-FLOOD; flood mapping and monitoring; Google Earth Engine; CEMS; multi-temporal

Citation: Lahsaini, M.; Albano, F.; Albano, R.; Mazzariello, A.; Lacava, T. A Synthetic Aperture Radar-Based Robust Satellite Technique (RST) for Timely Mapping of Floods. *Remote Sens.* **2024**, *16*, 2193. https://doi.org/10.3390/rs16122193

Academic Editors: Paraskevas Tsangaratos and Andrés Navarro

Received: 11 April 2024
Revised: 13 May 2024
Accepted: 14 June 2024
Published: 17 June 2024

1. Introduction

Floods are the most frequent and costly natural hazard worldwide, causing fatalities and significant economic damage in both rural and urban environments [1]. According to the Emergency Events Database, floods were the most common natural hazards in 2022, with 176 large events occurring worldwide, approximately 8000 deaths, and more than 57 million people affected [2]. Unfortunately, global temperature increases are generating widespread shifts in weather systems, making events such as floods more frequent, intense, and unpredictable [3]. The timely detection and monitoring of flood-prone areas are crucial for effective disaster management and response [4]. In recent years, remote sensing (RS) technologies have emerged as powerful tools for flood monitoring, with Synthetic Aperture Radar (SAR) at the forefront [5].

SAR imagery has indeed proven to be a powerful and effective approach for flood mapping [6–8]. Unlike optical sensors, SAR can penetrate clouds, rain, and vegetation, providing all-weather and all-day imaging capabilities [9], thus allowing for the detection

and characterization (extent, dynamics, and severity) of flooded areas at high spatial resolution [10–13].

The main limitation, especially in the past, of using SAR data for flood detection and monitoring purposes, namely their low temporal resolution, has been recently addressed by the implementation of several constellations of satellites sharing the same payload and orbit with a phase shift that allows for at least half of the temporal resolution when two satellites are present [14]. An example of such a constellation is represented by the Sentinel-1A (S-1A) and Sentinel-1B (S-1AB) satellites, which belong to the European Space Agency (ESA) Copernicus program and are equipped with a SAR system operating in the C-band (5.6 GHz) [15]. Each SAR has a spatial resolution of 10 m, while the nominal temporal resolution of each of the two S1 satellites is 12 days, which is reduced to six days when the two satellites are working together. This resolution increases at higher latitudes and over Europe, which are sampled more frequently than other locations in the world [14].

Various approaches have been employed for flood mapping using SAR imagery [8,10–21]. One commonly employed method is image differencing, which involves comparing pre- and post-flood SAR images to identify changes in the backscattering characteristics [12,13,16]. This approach was recently used by Hung and Jin [22], who analyzed multi-temporal Sentinel 1 data and highlighted the relevance of temporal analysis for effectively detecting and mapping floods. However, it is important to note that flood-affected pixels may exhibit signals similar to other features, such as high-altitude regions or shadows [18]. Thresholding is another approach in which a threshold value is set to distinguish between flooded and non-flooded areas based on the SAR image intensity values. Pixels above the threshold are classified as flooded, while those below are classified as non-flooded. This technique was recently applied to the historical Sentinel 1 data by Uddin et al. [23] for rapid flood mapping. However, this method has limitations when it comes to detecting water through dense vegetation [18]. Machine learning and data fusion techniques have been employed for flood mapping using Sentinel-1 data. Hitouri et al. [24] used training algorithms to classify flooded and non-flooded areas based on a combination of SAR data, ancillary data, and historical flood information. Another study by Gebrehiwot et al. [25] presented a method for flood extent mapping using an ensemble CNN model, further illustrating the use of advanced machine-learning techniques for flood detection. However, training these models requires large amounts of labelled data, which can be difficult to obtain.

This work introduces the SAR-Based Robust Satellite Technique-FLOOD (SAR-RST-FLOOD), a novel approach that utilizes SAR data to enable the accurate and timely detection of flooded areas. RST-FLOOD has been successfully applied to optical sensors data, such as those acquired by the Advanced Very High Resolution Radiometer (AVHRR), Moderate Resolution Imaging Spectroradiometer (MODIS), and Visible Infrared Imaging Radiometer Suite (VIIRS), to detect and monitor flood events by exploiting the typical behavior of water in the visible–near-infrared spectral region [26–28]. It is a multi-temporal approach aimed at the preliminary characterization of the investigated signal at the pixel level in unperturbed conditions, and then the identification of any signal transient as statistical deviation from these "normal" conditions [29]. In this study, the RST algorithm was applied for the first time to SAR data, particularly to backscattered signals, to identify flooded areas. One of the key advantages of the RST approach is its robustness against various environmental factors such as vegetation, topography, and weather conditions. On the other hand, one of the main limitations that has hampered the application of RST to SAR data so far is the computational effort, in terms of both data storage and processing, needed to analyze long-term series of backscatter signals over large areas.

In this study, we addressed this issue by leveraging the remarkable capabilities of the Google Earth Engine (GEE) cloud-based geospatial processing platform [30], which allowed us to implement our methodology in a streamlined and efficient manner. GEE revolutionizes the field of geospatial analysis by offering an intuitive and user-friendly interface, allowing us to explore and process data with ease while obtaining results at

both regional and global scales [30–33]. One of the key advantages of GEE is its ability to handle massive datasets, thereby facilitating informed decision-making and comprehensive analysis [26]. A remarkable feature of GEE is its vast geospatial data repository, which includes constantly updated Sentinel-1 GRD ("Ground Range Detected") data [14]. The availability of analysis-ready SAR datasets in GEE has greatly simplified the complex SAR pre-processing procedures, opening new avenues for SAR-based geospatial analysis.

SAR-RST-FLOOD was implemented in GEE, allowing us to develop an automatic method that can be applied anywhere. To validate the effectiveness of the proposed algorithm, extensive experimental evaluations were conducted using Sentinel-1 SAR data from different satellite missions, including the Copernicus Emergency Management System (CEMS) Mapping database [34]. The results demonstrate that the algorithm is highly accurate in detecting flooded areas and can provide timely information to aid disaster response and management efforts.

2. Materials

Several data were used in this study to implement the proposed methodology and assess its performance. A comprehensive list of the considered data, together with their main characteristics, is presented in Table 1, and their description is provided in the following subsections.

Table 1. List of data used.

Datasets	Raw Data	Spatial Resolution	Source of Data
SAR-image	Sentinel 1(GRD)	10 m	Copernicus
Hydrosheds	Based on SRTM	90 m	USGS
MERIT Hydro	Based on G1WBM, GSWO, and OSM	90 m	NASA
GSW	Global surface water	30 m	JRC
DEM	Digital elevation map	10 m	Grass site
TIF files	Ground data	Shapefile (.shp)	CEMS
Maps	Reference maps	60 m/30 m/10 m	CEMS

2.1. GEE Data and Derived Products

In this study, we used various freely available datasets from Google Earth Engine to enhance the research. Specifically, we analyzed data from the Sentinel-1 satellite mission, which has already been used for diverse Earth observation applications, including flood detection [35,36]. For our research, we employed the Interferometric Wide Swath (IW) mode of the S-1 mission, utilizing the VH polarizations (vertical–horizontal), which are more sensitive to changes on the land surface [37]. The IW mode provides extensive coverage and high-resolution imagery, making it suitable for flood detection and mapping [38]. The use of Sentinel-1 data, with its wide coverage, high-resolution imagery with a 10 m resolution, and frequent temporal updates, enabled us to conduct robust flood detection and mapping in the investigated study areas.

Moreover, we employed the HydroSHEDS Digital Elevation Model (DEM) to mask pixels representing steep land surfaces [39]. The inclusion of topographic information through the DEM allowed us to refine the flood mapping process and focus on areas where flooding is more likely to occur, enhancing the reliability of our results. We also relied on the JRC Global Surface Water (GSW) Mapping Layers dataset, which provides comprehensive maps of surface water location and temporal distribution from 1984 to 2020 [40]. This dataset also offers valuable statistics on the extent and changes of water surfaces over time. By leveraging this dataset and incorporating seasonality information, we aimed to accurately delineate and analyze the distribution of permanent and semi-permanent water bodies, contributing to a better understanding of global surface water dynamics. Finally, we used the MERIT Hydro dataset [41] to obtain a global flow direction map at a high resolution of 3 arcsec.

2.2. Reference Flood Data/Maps

To validate our flood detection methodology, we collected reference flood data from the Copernicus Emergency Management Service [34]. The reference data consisted of various types of information, including ground data on floods in TIF format and maps generated using ESRI World Imagery, COSMO-SkyMed, Radarsat-2, and other satellite images, including Sentinel ones. The flood maps in the TIF file provided precise geographic boundaries of the flooded areas, allowing for an accurate comparison and evaluation of the flood detection results. These shapefiles contain detailed information on the extent and location of the flood-affected areas. Where this information is not available, flood maps produced using other satellite images provided a visual representation of the events. These maps have often been produced by studying Sentinel 1 images, and where possible, we considered the same data to compare results.

3. Test Cases

Five different test cases were analyzed in this work to be representative of a wider range of conditions, considering the main features of the involved areas/rivers, as well as the events dynamic and damage. In addition, reference information was available for all these events, making them suitable for our analysis. The main information on the investigated events is reported in Table 2, where we also indicate the information of the S1 image processed to produce the results. It is clear that more data (before, during, and after the event) could have been used to better describe the dynamics of the events in the multi-temporal domain; however, this kind of analysis is beyond the scope of this paper.

A brief description of each event, the localization of which is shown in Figure 1, is presented below.

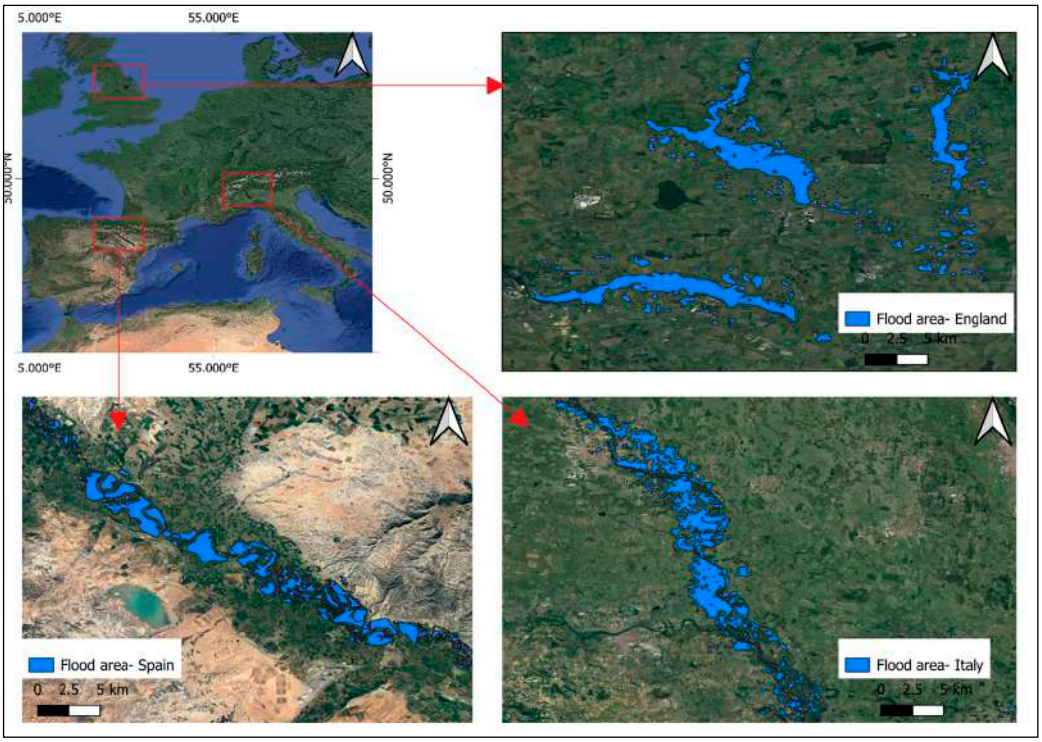

Figure 1. Localization of the study area. Flooded areas, as detected by CEMS, are shown in blue.

Table 2. Characteristics of the Sentinel-1 SAR images used in the study areas.

Study Areas	Event Date	Image	Mission Identifier	Date of Acquisition	Acquisition Mode
Spain (Zaragoza)	10 December 2021	After Flood	Sentinel-1A	16 December 2021	Descending
Spain (Tudela)	12 April 2018	After Flood	Sentinel-1A	13 April 2018	Descending
Spain (Zaragoza)	2 February 2015	During Flood	Sentinel-1A	2 February 2015	Descending
UK (Selby)	27 December 2015	After Flood	Sentinel-1A	29 December 2015	Descending
Italy (Sesia)	3 October 2020	During flood	Sentinel-1A	3 October 2020	Descending

3.1. Ouse River—England 2015

A severe storm affected the norther area of England on 27 December 2015. This storm brought heavy rainfall, with a 24 h total of 168 mm, affecting various areas such as York and Selby in the Yorkshire region [42]. The Ouse River and the Calder and Aire Rivers in West Yorkshire experienced significant flooding (Figure 1), affecting several cities, including Bradford and Leeds. The impact was substantial, with 7574 homes in northern England losing power at 08:00 on December 27. Notably, approximately 5500 of these homes were in the town of Rochdale in Greater Manchester, where a major electricity substation was flooded [43].

3.2. Sesia River—Italy 2020

The second study area focuses on the Sesia River, situated in the northern part of Italy. In October 2020, the area experienced an exceptionally severe meteorological event. Regional and National Civil Protection authorities responded by issuing red and orange alerts, respectively [44].

The northern and western parts of the Piedmont region were particularly affected with significant damage. Heavy rainfall has led to the overflow of multiple rivers and subsequent flooding of numerous areas [45]. In particular, the Sesia River experienced a breach that resulted in road closures, bridge collapses, and the submergence of various regions.

3.3. Ebro River—Spain (2015, 2018, 2021)

In recent years, several events have affected the Ebro River in Spain (2015, 2018, and 2021). The river stretches 930 km (approximately 580 miles) from the Cantabria Mountains to the Mediterranean Sea, playing a crucial role in the surrounding areas and the whole of Spain.

In February 2015, the Ebro River experienced major flooding in the Zaragoza region. The river flow rate reached an impressive 2400 cubic meters (84,700 cubic feet) per second during this event. The swollen river cut through Zaragoza, affecting approximately 700,000 people and submerging large areas of nearby farmland [46].

In April 2018, the Ebro River threatened the city of Tudela. Due to snowmelt in river catchment areas and a period of heavy rain, the river's rising waters prompted authorities to issue an orange alert at the second-highest level on the Spanish scale [39]. The water level reached over five meters before gradually receding [47]. It is worth noting that the water level was lower than that recorded in 2015 only because of the measures taken to improve the safety of the populations closest to the channel after the 2015 event [48].

Another flood affected Zaragoza in December 2021. This flood was triggered by heavy rainfall and rapid snowmelt over a 72 h period, leading to extensive damage and disruption in the upper and middle Ebro River basin that runs through Zaragoza. Spain's Meteorological Agency (AEMET) reported that on 10 December, the Arga River in Pamplona reached 4.80 m, whereas the Ebro River in Castejón reached 7.94 m by 11 December. Flooding along the Ebro later affected areas of the Aragon region, including the capital Zaragoza, where the river reached 5.52 m on 14 December 2021 [49]. Areas along the river in the city were flooded, and the Spanish Red Cross reported that patients from a hospital in the city were evacuated [49]. Unfortunately, these floods highlight the increasing frequency of such events in Spain due to climate change. Authorities continue to monitor

and take precautionary measures to mitigate the impact of future floods in Zaragoza and its surrounding areas.

4. The RST Approach

The RST algorithm is an automatic multi-temporal change-detection method that has been extensively tested for detecting various environmental hazards [29,50]. The method is based on the preliminary identification of "normal" (i.e., unperturbed) values of the investigated signal that should be compared with the signal at hand for the detection of any significant, from a statistical point of view, anomalies. Such an analysis is performed at the pixel level and requires the preliminary generation of a homogeneous long-term satellite database. Homogeneity in the spatial domain is ensured by always considering the same area (and pixels), whereas homogeneity in the temporal domain is ensured by collecting data belonging to the same calendar month and acquired at the same time of day (or in the same orbit). The change detection step is performed by implementing the Absolutely Local Index of Change of Environment (ALICE) index (1), as in the following [50]:

$$\otimes_V(x,y,t) = \frac{V(x,y,t) - \mu_V(x,y)}{\sigma_V(x,y)} \quad (1)$$

where $V(x,y,t)$ is the signal measured at time t for each pixel (x,y) of the analyzed satellite scene, and $\mu_V(x,y)$ and $\sigma_V(x,y)$ represent the temporal mean and standard deviation, respectively, which are computed by processing the above-mentioned homogeneous multi-temporal dataset of the collected satellite data [29]. The Alice index, by its inherent design, is intended to be a standardized variable that exhibits Gaussian behavior, with a mean close to 0 and a standard deviation close to 1. Consequently, a higher absolute value of the index indicates a lower probability of its occurrence [50].

In its first implementation on SAR data, performed in this work, the signal under investigation is the backscatter measured by Sentinel 1, with the prescriptions for the used data indicated as follows. It is worth mentioning that the backscatter intensities are influenced by the characteristics of the surface, including its roughness, composition, and presence of water. In the absence of flooded areas, these characteristics can be considered constant if the same pixel is viewed with the same geometry during the same period of the year. Therefore, in the absence of any other perturbations, signal anomalies, if detected, can be related to the presence of flooded areas. Considering the incidence angle, its similarity along the temporal series accounts for shadowing and layover effects, enabling accurate differentiation between flooded and non-flooded regions [51]. As already mentioned, the RST approach implementation requires computational capability to increase on the basis of the spatiotemporal and resolution of the investigated data, as well as on the length of the historical series analyzed. These factors, together with the limited accessibility of radar data, have prevented the application of RST to raw SAR data. This study represents the first attempt to analyze a historical series of backscatter values following RST prescriptions and exploit its inherent advantages.

5. The Methodology

The workflow followed in this study was implemented using the Google Earth Engine platform and deploying the JavaScript programming language. The workflow was divided into five stages (Figure 2), described in the following, to ensure a systematic and comprehensive approach to flood detection (Figure 2).

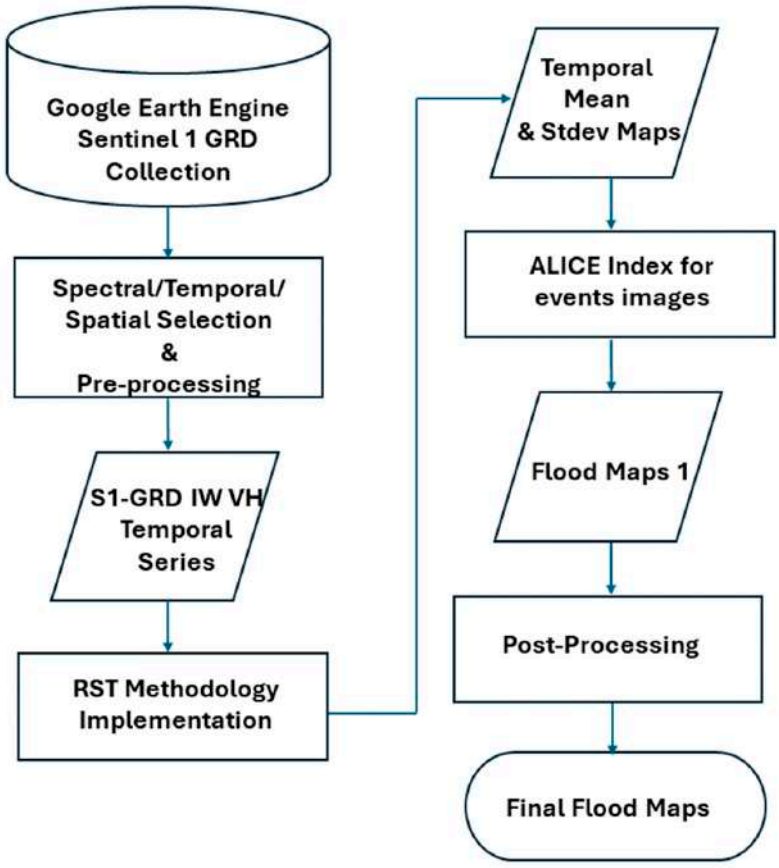

Figure 2. SAR-RST-FLOOD approach flowchart.

5.1. Sentinel-1 Data Selection and Pre-Processing

The main features of the used Sentinel-1A and 1B have already been mentioned. By exploiting the GEE platform, IW GRD scenes with VH polarization were selected for the areas under investigation. Temporal selection was performed by focusing on the month/s of event/s analyzed in a multi-temporal framework. To ensure the reliability of our results, we implemented a filtering process to exclude poor-quality images from the collection. This step was crucial to avoid potential inaccuracies and inconsistencies in the data used in the analysis. A total of 475 images stratified based on the calendar month of event occurrence were analyzed.

Several pre-processing steps were automatically executed within the GEE platform to enhance SAR image quality. These steps include thermal noise removal, data calibration, multi-looking, and range Doppler terrain correction. However, to further improve SAR data quality, additional pre-processing steps are necessary. The Committee on Earth Observation Society (CEOS) Analysis-Ready-Data for Land (CARD4L) recommends several supplementary pre-processing techniques, including border noise removal, speckle filtering, and radiometric terrain correction [52]. For speckle filtering, we employed the Refined Lee filter [53], which was originally introduced by [54], and we used this filter at a kernel size of 7×7. To address the influence of topography on SAR backscatter, we implemented radiometric terrain correction based on the approach proposed by Hoekman and Reiche [55], as implemented by [56,57]. This approach incorporates an angular-based correction that considers the angular relationships between the SAR image and terrain geometry. We utilized the SRTM dataset at a resolution of 1 arc-second (30 m), which is readily available in GEE [58]. The latter was replaced by our DEM with a higher resolution of 10 m, where it was available. The primary objectives of these pre-processing steps are to mask and exclude pixels located in the active layover and shadow areas of the image [55,59]. Following the

completion of the pre-processing steps, we converted the output to a logarithmic scale of dB. This conversion facilitates clearer visualization and enhances image interpretability.

5.2. RST Methodology Implementation

The historical series of S1-GRD images with VH polarization was used as the input to implement the RST methodology. As described above, such an activity encompasses two main steps: (i) the identification of the expected values at the pixel level (i.e., temporal mean and standard deviation) for the investigated signal (i.e., the backscattering σ0); (ii) and the ALICE index computation for all the S1 images useful to characterize the analyzed flood events.

In Figure 3, two examples of the ten maps (one temporal mean map plus one standard deviation map for five events) produced in the first step are shown. These maps refer to the two outputs produced for analyzing the Zaragozza Ebro River event (December 2021). They were obtained by analyzing at the pixel levels all S1 GRD IW data collected in the calendar month of December from 2014 to 2023. Similar maps, which are not shown for the sake of brevity, were produced for all other events.

Using these maps as reference signals, the ALICE maps for all images in Table 2 were computed, highlighting values higher than two, whose probability of occurrence was less than 3% for inherent construction [29,50]. These maps were used as inputs in the next step to produce the final flood maps.

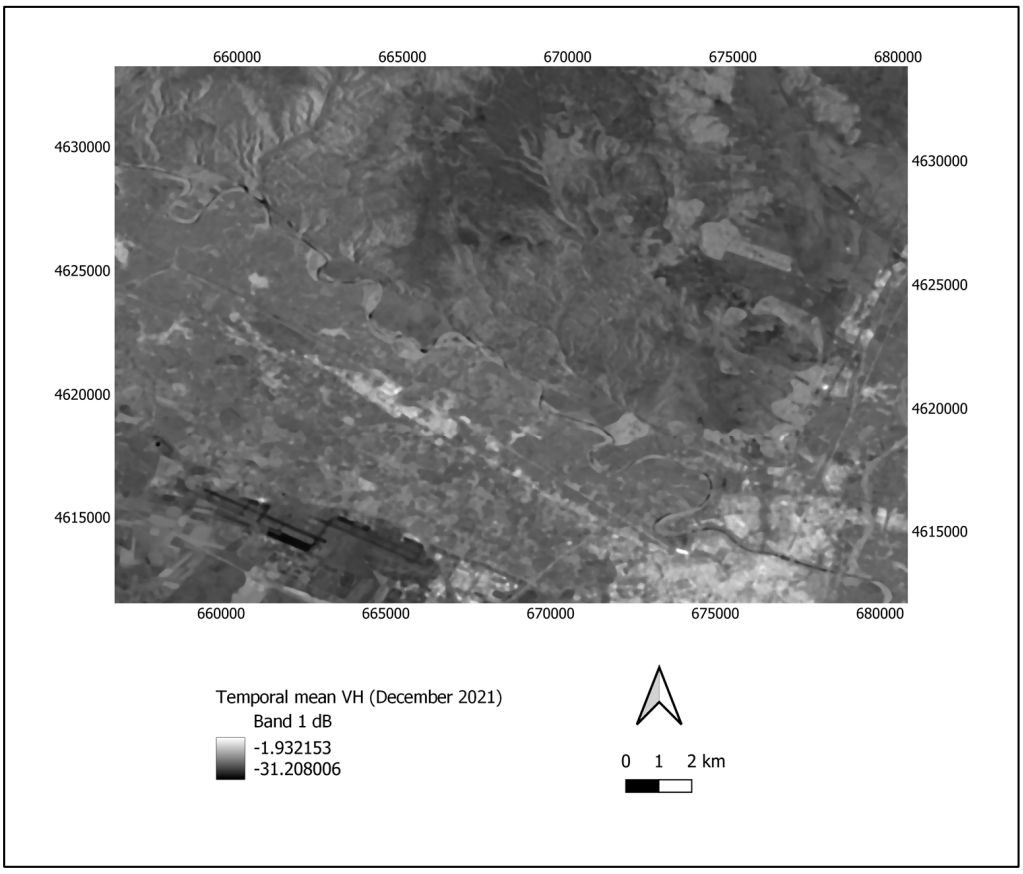

(**a**)

Figure 3. *Cont.*

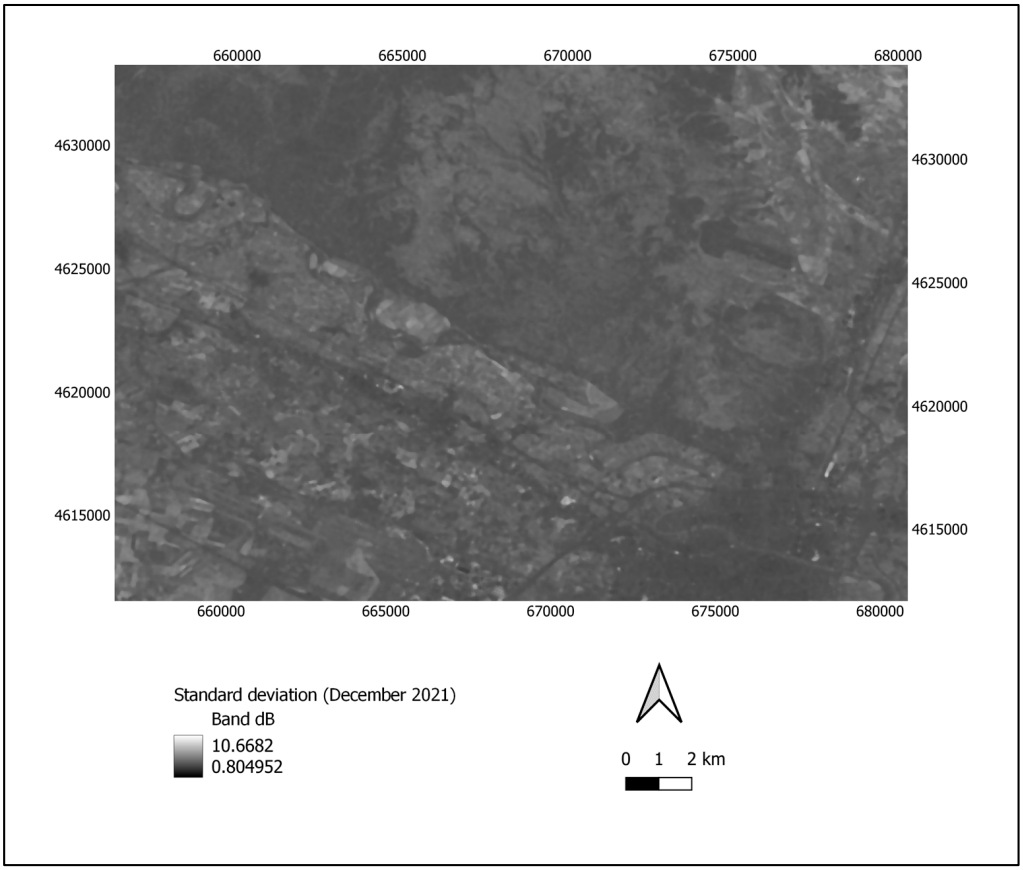

(**b**)

Figure 3. Maps of multi-temporal (December 2014–2023) (**a**) temporal mean and (**b**) standard deviation, computed for the Zaragozza Ebro River event.

5.3. Post-Processing

To enhance the quality of the flood extent layer and reduce the number of false positives, we used additional datasets and applied post-processing steps. First, we used the global surface water dataset (GSW) [40] to distinguish between permanent and semi-permanent water bodies. This dataset provides comprehensive maps of surface water location and temporal distribution and offers valuable statistics on the extent and changes in water surfaces over time. To identify areas with permanent or semi-permanent water bodies, we used the seasonality band within the dataset. This band provides information on seasonality, ranging from 0 to 12 months, allowing us to effectively mask out areas with consistent water presence throughout the year. By leveraging this dataset and incorporating seasonality information, we aimed to accurately delineate and analyze the distribution of permanent and semi-permanent water bodies, contributing to a better understanding of global surface water dynamics.

We then employed topographic filtering techniques based on the elevation data from the DEM obtained from the HydroSHEDS dataset [39]. By setting a threshold slope percentage, we identified areas where the slope exceeded a certain value. These steep areas were considered unsuitable for flooding because water naturally flows away from them. By filtering these incorrectly flooded pixels, we aimed to improve the accuracy of our flood detection analysis. The inclusion of topographic information through the DEM allowed us to refine the flood mapping process and focus on areas where flooding is more likely to occur, enhancing the reliability of our results.

Additionally, we used information provided by the MERIT hydro dataset [41]. To detect permanent water bodies, we focused on the "wet" band, where land areas are represented by 0 and permanent water bodies by 1. Furthermore, using this dataset, we

implemented a 2 km buffer to specifically highlight rivers while eliminating any false positive water detections. This approach allowed us to accurately identify and visualize river networks while ensuring the exclusion of non-river water features.

5.4. Validation

The final step of this study involved validating the processed flood extent maps generated in previous stages. The accuracy of the SAR-RST-FLOOD approach was assessed using various methods and a range of reference datasets, including reliable flood information from CEMS.

We assessed the accuracy of the flood maps by comparing them with the same Sentinel-1 imagery taken on the same date using another approach, such as the automatic threshold method provided by the CEMS. In cases where we were unable to find a Sentinel 1 image for the same date, we assessed the accuracy of the flood maps by comparing them with different types of images, including ESRI World Imagery, COSMO-SkyMed, Radarsat-2, and other satellite images, and then with the provided ground truth information regarding floods in the TIF files containing flood extents. Through these rigorous validation processes, we aimed to ensure the reliability and precision of the flood mapping results obtained using the SAR-RST-FLOOD approach.

The agreement between the two mapping approaches was assessed using a confusion matrix that served as a concise summary of the classification model predictions, indicating the numbers of correct and incorrect predictions. By analyzing the values in the confusion matrix, various metrics were calculated to assess the agreement between the two mapping approaches ([18], such as the user's (UA), producer's (PA) and overall accuracy (OA), as well as the Kappa index (K), as described in the following.

$$\mathrm{UA_f} = \frac{A}{A+B} \tag{2}$$

$$\mathrm{UA_{nf}} = \frac{D}{C+D} \tag{3}$$

$$\mathrm{PA_f} = \frac{A}{A+C} \tag{4}$$

$$\mathrm{PA_{nf}} = \frac{D}{B+D} \tag{5}$$

$$\mathrm{OA} = \frac{A+D}{A+B+C+D} \tag{6}$$

$$\mathrm{K} = \frac{\frac{A+D}{A+B+C+D} - \frac{(A+B)(A+C)+(C+D)(B+D)}{(A+B+C+D)^2}}{1 - \frac{(A+B)(A+C)+(C+D)(B+D)}{(A+B+C+D)^2}} \tag{7}$$

where A is the number of pixels considered flooded by both the RST and the reference map, B and C are the "False" negative or positive RST detection (considering the reference map as the true), and D represents the pixels that were not recognized as flooded by both methods. In Equations (2) and (4), f is for "flooded", whereas in Equations (3) and (5), nf is for "not flooded".

6. Results

Flood mapping was conducted for each investigated flood event, serving as a valuable tool for assessing our approach. In the following subsections we provide regional-scale flood maps, offering both an overview and a detailed perspective of the five study areas. In each map, in addition to the involved river/s and its/their main flow direction (black arrow), the SAR-RST-FLOOD and reference data outputs are plotted in different colors.

6.1. Ouse River—England 2015

The CEMS system was activated for this event on 28 December 2015 [60]. We considered the flood delineation map generated by analyzing a RADARSAT image acquired on 29 December 2015 as reference data for this case study. The flood map was generated by CEMS using a semi-automatic approach with an estimated geometric accuracy of 10 m [60]. This reference map was then compared with the SAR-RST-FLOOD map computed on the same date (Figure 4).

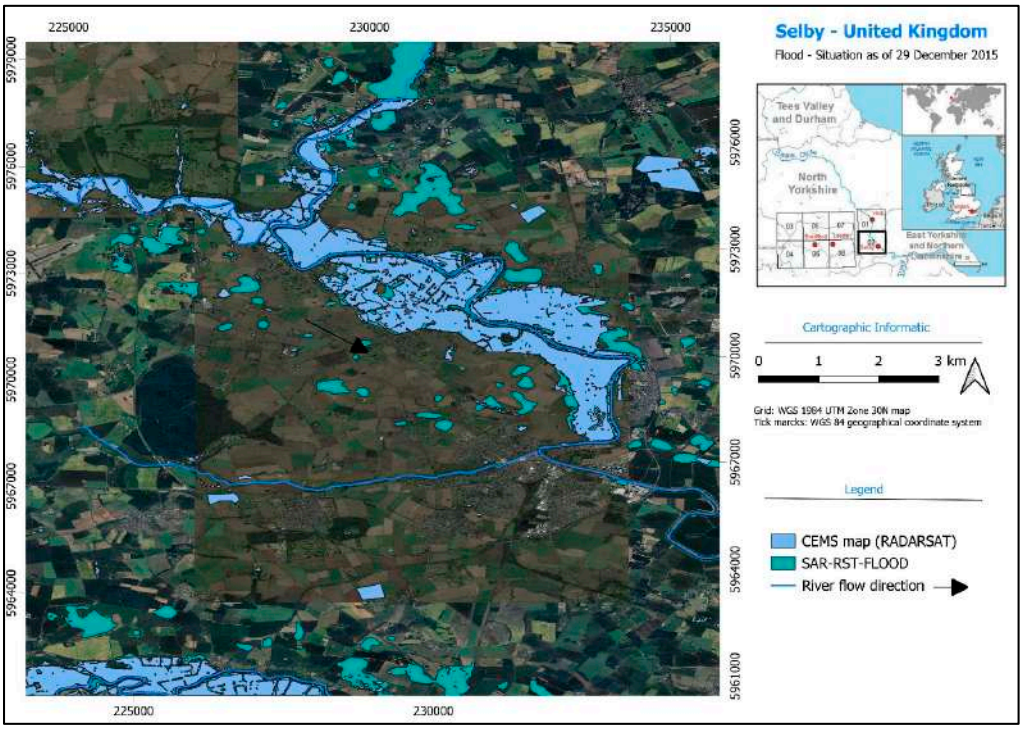

Figure 4. Flood Map of the Ouse River event (29 December 2015).

The user accuracy value was 0.64, the produced accuracy was 0.98, and the Kappa index reached 0.77 (Table 3). From the image (Figure 4), it is evident that the proposed approach was able to detect more flooded pixels than those achieved by applying the threshold method to the RADARSAT image. Such a discrepancy, whose reliability cannot be assessed in the absence of ground data, is mostly related to the difference between the two used methods. In any case, the high Paf value indicates the good reliability of the RST approach.

Table 3. Confusion matrix for the Ouse River event (29 December 2015).

Event 1: England Flood 27 December 2015		**Reference Data**		**Accuracy Matrix**				
		Flood	Not Flooded	UA_f	UA_{nf}	PA_f	PA_{nf}	K
RST-SAR-FLOOD	Flood	681,574	306,425	0.64	0.92	0.98	0.72	0.77
	Not Flooded	39,209	10,312,432					

6.2. Sesia River—Italy 2020

The CEMS system was activated for this event on 4 October 2020 [61]. The first estimate product generated by analyzing a Sentinel 2 image acquired on 3 October 2020 was considered the reference data for this case study. The flood map was generated using CEMS from an image by means of visual interpretation, with an estimated geometric accuracy (RMSE) of 7.5 m [61]. The SAR-RST-FLOOD map (Figure 5) was produced by considering the Sentinel 1 image collected on the same date.

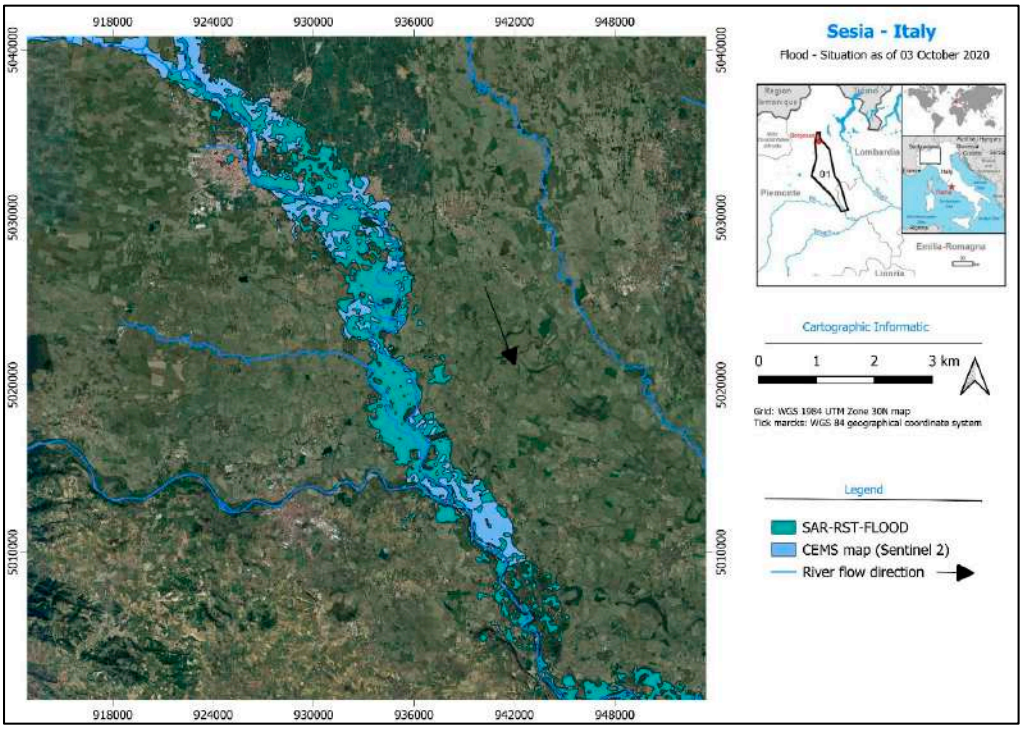

Figure 5. Flood map of the Sesia River event (3 October 2020).

The user accuracy was relatively lower at 0.58, in contrast to other parameters, such as UAnf (0.92), PAf (0.98), and K (0.68) (Table 4). One factor contributing to the lower UAf is the inherent lack of direct comparability between the SAR and Sentinel 2 maps. This disparity arises because the SAR maps undergo topographic correction, allowing the detection of flood areas in vegetated zones that are undetectable by Sentinel 2. In addition, the method used for assessing flooded extension on the reference data may have added some uncertainty.

Table 4. Confusion matrix for Sesia River event (3 October 2020).

Event 2: Italy Inundation 3 October 2020		**Reference Data**		**Accuracy Matrix**				
		Flood	Not Flooded	UA_f	UA_{nf}	PA_f	PA_{nf}	K
RST-SAR-FLOOD	Flood	340,879	148,082	0.58	0.95	0.96	0.97	0.68
	Not Flooded	23,669	4,672,132					

6.3. Ebro River—(Zaragoza) Spain 2015

The CEMS system was activated for this event on 2 February 2015 [62]. For this case study, we considered a flood delineation map generated by analyzing a Sentinel 1 image acquired on 3 February 2015. The flood map was produced by CEMS using a semi-automatic approach, also considering visual interpretation, with an estimated geometric accuracy (RMSE) of 15 m and a thematic accuracy of 85% [62]. The SAR-RST-FLOOD map was produced using the same Sentinel 1 image (Figure 6).

The user accuracy reached 0.76, Paf reached 0.98, and the Kappa index reached 0.84 (Table 5). This notable accuracy is related to the similarity between the maps (Figure 6), and both were corrected topographically. In addition, in this case, the visual analysis of the two images shows some discrepancies between the two outputs, which cannot be better investigated in the absence of a ground truth.

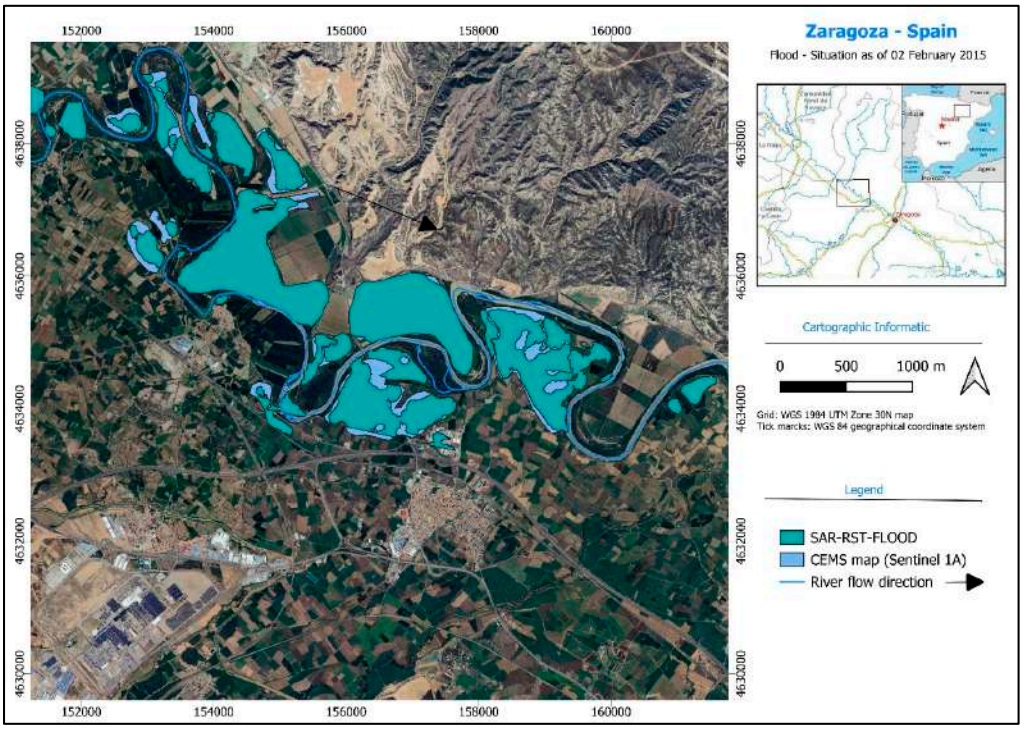

Figure 6. Flood map of the Ebro River (Zaragozza) event (2 February 2015).

Table 5. Confusion matrix for Ebro River (Zaragozza) event (3 February 2015).

Event 3: Zaragoza Inundation 2 February 2015		Reference Data		Accuracy Matrix				
		Flood	Not Flooded	UA_f	UA_{nf}	PA_f	PA_{nf}	K
RST-SAR-FLOOD	Flood	237,392	71,737	0.76	0.97	0.98	0.81	0.84
	Not Flooded	10,921	2,540,721					

6.4. Ebro River—(Tudela) Spain 2018

The CEMS system was activated for this event on 13 April 2018 [63]. The flood delineation map generated by using a semi-automatic approach for the COSMO-SkyMed images acquired on 13 April 2018 at 17:45:11 UTC and 17:45:16 UTC) and by means of visual interpretation due to the poor radiometric quality of the COSMO-SkyMed data acquired on 13 April 2018 at 18:09:16 UTC and 18:09:21 UTC was considered as the reference data for this case study. The estimated geometric accuracy was 5 m [63]. The flood extension analysis involved a comparison between this map and the SAR-RST-Flood one generated by analyzing a Sentinel 1 image acquired on 13 April 2018 (Figure 7).

UAf exceeded 0.94, indicating reasonably accurate flood extent mapping, the PAf value was 0.69 and K was 0.84 (Table 6). The two outputs (Figure 7) appear to be very similar, indicating the high reliability of the RST approach.

Table 6. Confusion matrix for Ebro River (Tudela) event (13 April 2018).

Event 4: Tudela Inundation 13 April 2018		Reference Data		Accuracy Matrix				
		Flood	Not Flooded	UA_f	UA_{nf}	PA_f	PA_{nf}	K
RST-SAR-FLOOD	Flood	23,728	6963	0.94	0.95	0.69	0.76	0.75
	Not Flooded	1102	253,972					

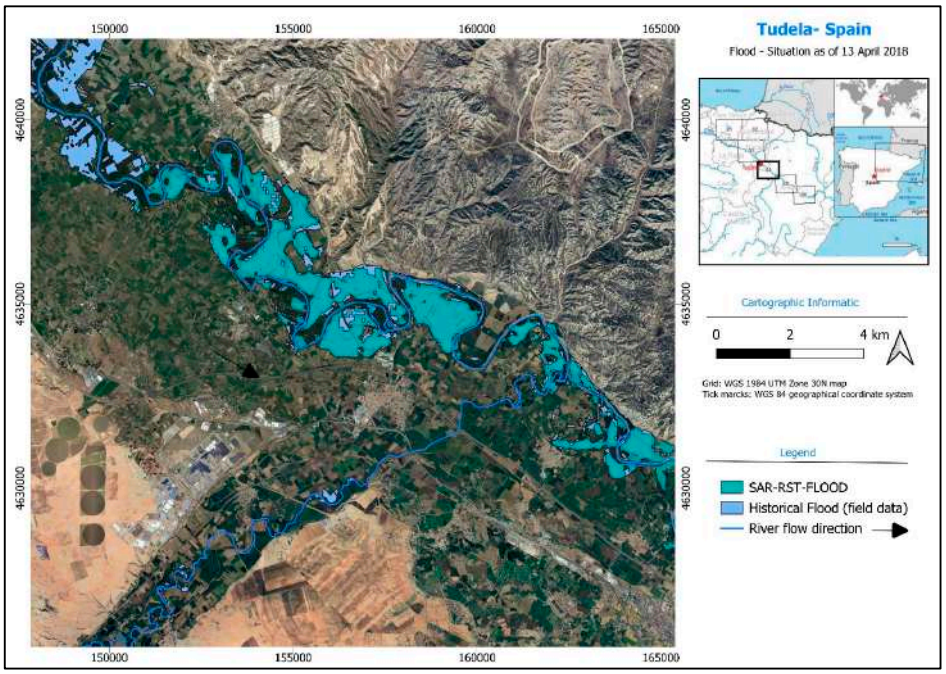

Figure 7. Flood map of the Ebro River (Tudela) event (13 April 2018).

6.5. Ebro River—Zaragoza, Spain 2021

The CEMS system was activated for this event on 10 December 2021 [64]. The flood delineation map generated by analyzing RADARSAT 3 data acquired on 15 December 2021 was considered as the reference data for this case study. The flood map was generated by CEMS using a semi-automatic approach, with an estimated geometric accuracy (RMSE) of 20 m [64]. This reference map was compared with the SAR-RST-FLOOD map computed by investigating the Sentinel 1 image acquired on 16 December 2021.

UAf exceeded 0.97, indicating accurate flood extent mapping; the PAf value was 0.87 and K was 0.87 (Table 7). A high level of agreement was found between the two maps (Figure 8) despite the high level of vegetation surrounding the river.

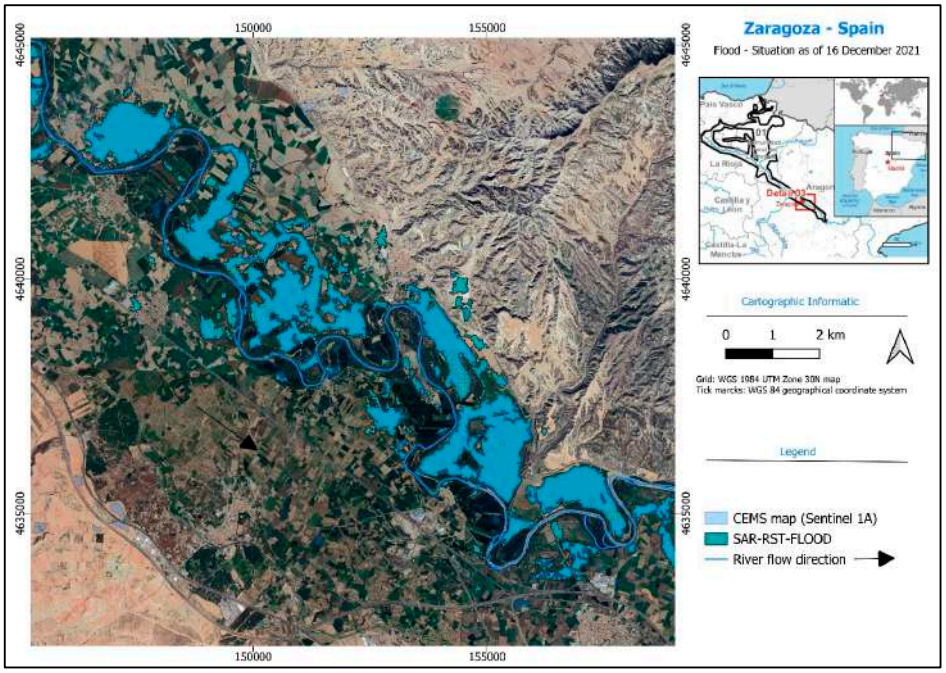

Figure 8. Flood map of the Ebro River (Zaragozza) event (16 December 2021).

Table 7. Confusion matrix for the Ebro River (Zaragozza) event (16 December 2021).

Event 5: Zaragoza Inundation 10 December 2021		Reference Data		Accuracy Matrix				
		Flood	Not Flooded	UA_f	UA_{nf}	PA_f	PA_{nf}	K
RST-SAR-FLOOD	Flood	360,790	147,090	0.97	0.95	0.87	0.90	0.87
	Not Flooded	24,790	4,762,093					

7. Discussion

SAR data have been largely used for flood detection purposes owing to their capability to provide detailed all-day and all-weather information. The Copernicus program, as well as the Cosmo Sky Med mission [65] have facilitated the acquisition of data with good temporal resolution, owing to the presence of several satellites sharing the same payload. One residual limitation related to the intensive computational tasks related to the pre-processing of SAR data, especially when long-term series are analyzed, has been recently faced thanks to the availability of advanced computing platforms, such as Google Earth Engine.

In this study, GEE has facilitated the implementation of a multi-temporal approach, RST-FLOOD, on a historical series of S1 data to map different flooding events that have occurred in Europe in recent years. Among the dozen events available, whose analysis would have clearly not been feasible and out of the scope of the study, we selected five flood episodes representative of a wider range of characteristics in terms of the area affected, precipitation, and damage. Moreover, detailed reference data were available for these events, making them useful in terms of assessing the accuracy of the proposed methodology. To this end, in the absence of in situ data, we used other maps and information made available by the Copernicus Emergency Mapping System. In any case, it is worth saying that accurate ground measurements of flood extent are difficult to obtain because of meteorological and safety conditions [66], and they are usually collected with a time delay with respect to satellite acquisition, which could lead to misclassification due to flood dynamics [18]. Therefore, using remote sensing data/products as reference maps, such as those provided by the CEMS, still represents a viable alternative [14,17,18,67], even if also these products may lack accuracy depending on the quality and sensitivity of the considered data and method of analysis.

The obtained results, when compared with CEMS maps/information, indicate the feasibility of the proposed approach. In more detail, considering all the analyzed events together, a Kappa index value of 0.78 and an overall accuracy of 0.96 were found, suggesting the good reliability of the method. Similar confirmations arose from the analysis of the Uaf and Paf mean values, equal to 0.78 and 0.90, respectively. Such good results have been obtained notwithstanding several issues typically affecting the accuracy of flood disaster information [18], such as the high heterogeneity (spatial resolution, date of acquisition, etc.) of the considered reference maps, ranging from S1 images to S2, RADARSAT, and ground data, as well as the methods used for detecting flooded pixels. In any case, other events should be investigated in the future to further confirm such results. Owing to its implementation within the GEE platform, where all other ancillary data used to increase the quality of the results are also present, the proposed approach can be easily applied on a global scale and can provide crucial information for remote areas characterized by the presence of ungauged and/or poorly instrumented basins. In these areas, as well as for those where a violent and/or extreme event, such as a flood, can destroy the ground monitoring system, satellite data can represent the only source of information available [68]. Furthermore, the processing of dense SAR time series is performed in a short time, allowing for the rapid production of results. The technique is completely automatic and unsupervised and does not require a preliminary selection of a baseline or human support.

Once the accuracy of the proposed approach in mapping flood events was assessed, its potential for monitoring purposes was investigated. To this end, we analyzed the last of

the considered test cases in greater detail, i.e., the Ebro River event that occurred around Zaragozza in December 2021. Two other S1 images were available after the one of 16 December 2021, already analyzed (Figure 8). The first one was acquired on 17 December 2021 by S1A and the second on 22 December 2021 by S1B. The results of the RST-SAR-FLOOD application for these two images are shown in Figure 9a,b.

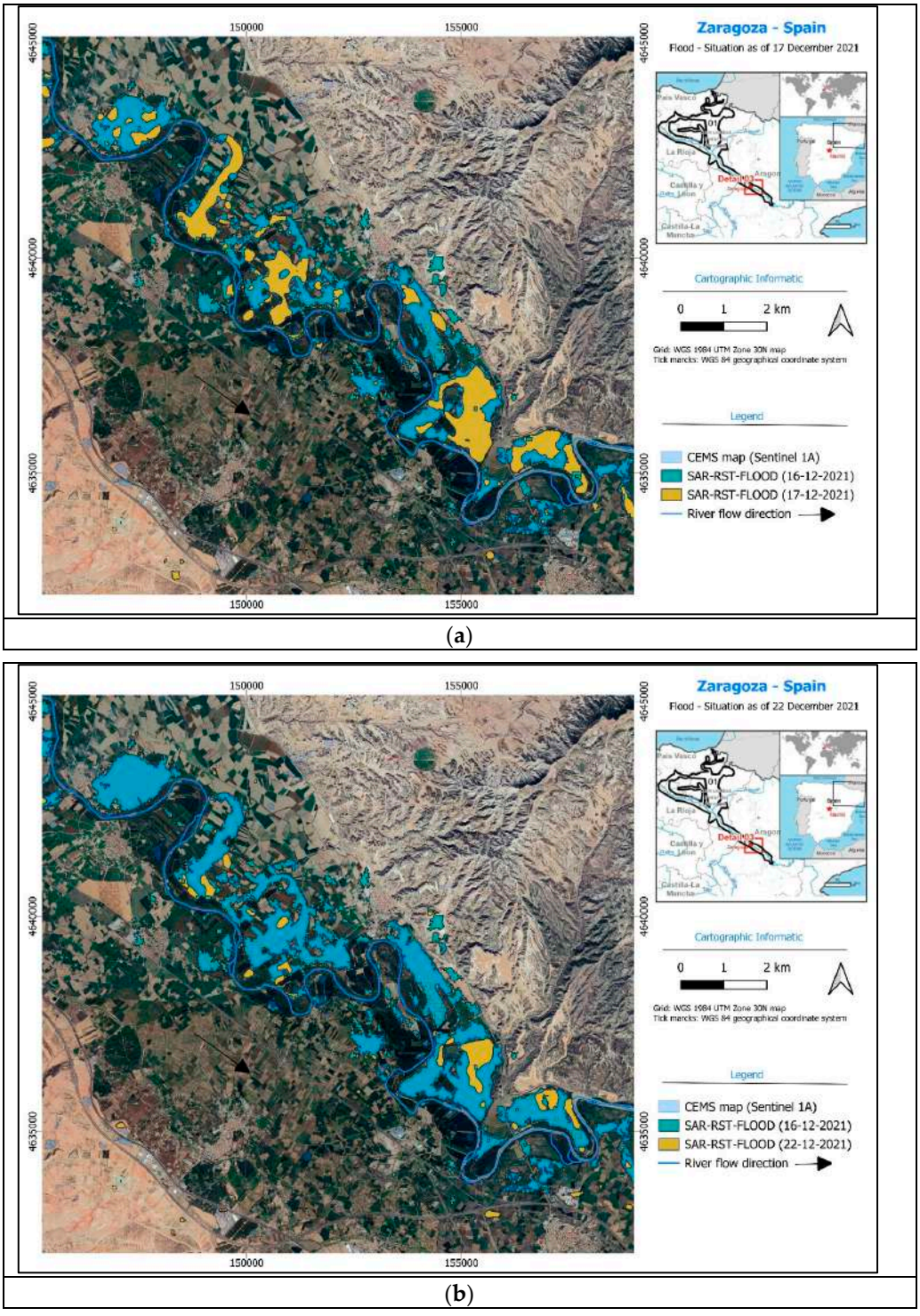

Figure 9. Flood maps of the Ebro River (Zaragozza) event for: (**a**) 17 December 2021; (**b**) 22 December 2021.

A clear reduction in the flooded areas is evident in the two maps, especially in the second one, highlighting the zones most affected by the flood, whose presence was still evident one week after the first detection. This information, typically acquired when a meteorological perturbation is still present and hence prevents optical data acquisition, is fundamental to better manage recovery actions, as well as to delineate clear flooding scenarios useful for implementing future mitigation activities.

The availability of more images, together with other information acquired remotely or in situ, such as the measurement of rainfall spatial and temporal variability, is fundamental for modelling and reconstructing catastrophic flooding events [68]. The integration of human observations (crowdsourced data) may further help to validate complex flooding events in data-scarce areas with unavailable gauged records [68–70]. Finally, it should be stressed that accurate indications about the areas affected by a flood event are fundamental to developing flood hazard maps that are useful for risk-aware analyses and designs [71]. In this context, the development of probabilistic approaches and stochastic techniques for flood hazard assessment may improve the definition of flood risk scenarios [71].

The implementation of the proposed methodology was made possible by the concurrence of two factors. The European Union's choice to make all the data collected within the Copernicus program open and freely available represents an innovative idea that has allowed for the growing use of these data in the everyday life of each kind of potential stakeholder, from local regional authorities to the general public [72], as well as the development of several downstream applications. This has been facilitated and accelerated by the development of cloud computing systems, such as GEE, which permits "easy" access to and processing of these data [33], overcoming one of the main barriers to a more systematic use of Copernicus data/products [72].

The potential limitations of the RST-SAR-FLOOD method may be represented by a reduced capability to investigate floods occurring in urban areas, mountainous regions, and coastal zones, where the discrimination between flooded pixels and others showing similar characteristics could be more complicated [18]. Another issue of the proposed approach is represented by the current temporal resolution of Sentinel 1 data. S1B, launched in April 2016, stopped working on 23 December 2021, soon after the acquisition of the image analyzed in Figure 9, due to a failure of the electronic power supply to the instruments [54]. The ESA is currently working on the launch of Sentinel-1C as soon as possible to re-establish the satellites constellation [73]. Until S1C will not be operational, the nominal temporal resolution of S1 mission will remain 12 days, limiting the capability of such a system in providing timely information about processes in progress on the surface of the Earth.

8. Conclusions

In this study, the RST-FLOOD method, which has already proven successful in detecting and monitoring flood events using optical data, was applied to Synthetic Aperture Radar (SAR) data for the first time. Sentinel 1 data, freely provided by the Copernicus program, were used for this aim, exploiting the potential of the Google Earth Engine platform. Five test cases were evaluated by comparing the results of the SAR-RST-FLOOD method with those provided by the Copernicus Emergency Mapping System. The user accuracy values ranged from 0.58 to 0.97, with an average value of 0.78, producing accuracy values from 0.69 to 0.98, with an average value of 0.90, and the K values ranged from 0.68 to 0.87, with an average value of 0.78.

These satisfactory results, achieved notwithstanding the discrepancies in terms of spatial resolution, time of acquisition, and method used between the two datasets, indicate the good performance of the proposed approach. Moreover, they highlight the main advantage of a multi-temporal approach, such as the one presented here, with respect to traditional techniques, namely its capability to automatically define local (i.e., at the pixel level) adaptive thresholds useful for the robust identification of flooded areas, reducing the occurrence of false detections. In addition, the strong capability of providing useful information about flood dynamics due to the good temporal resolution provided by the

S1 constellation, when fully operational, was also demonstrated. Frequently updated and accurate indications about flood extent during crises are crucial to overcoming the issues related to the poor accessibility of the areas affected by the event, as well as the potentially bad functionality of ground monitoring systems.

The high computing potential of the Google Earth Engine platform allows for the rapid generation of results, making the proposed approach suitable for near real-time activities in support of disaster monitoring and management activities. Timely and accurate information about flood extent and evolution is fundamental not only during the emergency phase, when they can allow for better management of the crisis by decision makers, but also in the recovery phase, to develop accurate flood hazard maps that are useful for mitigating the flooding risk for the areas affected by the flood. Considering that the developed system is already filled with all the information useful for its implementation, its potential to be applied on a global scale as well as to support the management of ungauged or remote basins are evident. Local and regional public authorities and institutions can take advantage of our research by integrating the information provided with those by traditional approaches to obtain a clearer understanding of the event in progress.

Future analysis will focus on assessing the capability of the SAR-RST-FLOOD approach to detect floods in urban areas, mountainous regions, and coastal zones, trying to implement a method that can be applied everywhere with a constant level of accuracy.

Author Contributions: Conceptualization, M.L. and T.L.; methodology, M.L. and T.L; software, M.L. and F.A.; validation, M.L.; formal analysis, M.L. and T.L.; writing—original draft preparation, M.L. and T.L.; writing—review and editing, R.A., A.M. and T.L.; supervision, T.L. All authors have read and agreed to the published version of the manuscript.

Funding: This research received no external funding.

Data Availability Statement: Publicly available datasets were analyzed in this study. These data can be found here: https://developers.google.com/earth-engine/datasets/catalog/COPERNICUS_S1_GRD (accessed on 9 April 2024).

Conflicts of Interest: The authors declare no conflicts of interest.

References

1. Doocy, S.; Daniels, A.; Murray, S.; Kirsch, T.D. The Human Impact of Floods: A Historical Review of Events 1980–2009 and Systematic Literature Review. *PLoS Curr.* **2013**, *5*. [CrossRef] [PubMed]
2. CRED. *Climate in Action Executive Summary*; EM-DAT the International Disasters Database; CRED: Brussels, Belgium, 2022; pp. 1–8.
3. Zhao, Q.; Yu, P.; Mahendran, R.; Huang, W.; Gao, Y.; Yang, Z.; Ye, T.; Wen, B.; Wu, Y.; Li, S.; et al. Global climate change and human health: Pathways and possible solutions. *Eco-Environ. Health* **2022**, *1*, 53–62. [CrossRef] [PubMed]
4. Finley, P.; Gatti, G.; Goodall, J.; Nelson, M.; Nicholson, K.; Shah, K. Flood Monitoring and Mitigation Strategies for Flood-Prone Urban Areas. In Proceedings of the 2020 Systems and Information Engineering Design Symposium (SIEDS), Charlottesville, VA, USA, 24 April 2020.
5. Voigt, S.; Kemper, T.; Riedlinger, T.; Kiefl, R.; Scholte, K.; Mehl, H. Satellite image analysis for disaster and crisis-management support. *IEEE Trans. Geosci. Remote Sens.* **2007**, *45*, 1520–1528. [CrossRef]
6. Matgen, P.; Hostache, R.; Schumann, G.; Pfister, L.; Hoffmann, L.; Savenije, H. Towards an automated SAR-based flood monitoring system: Lessons learned from two case studies. *Phys. Chem. Earth* **2011**, *36*, 241–252. [CrossRef]
7. Westerhoff, R.S.; Kleuskens, M.P.H.; Winsemius, H.C.; Huizinga, H.J.; Brakenridge, G.R.; Bishop, C. Automated global water mapping based on wide-swath orbital synthetic-aperture radar. *Hydrol. Earth Syst. Sci.* **2013**, *17*, 651–663. [CrossRef]
8. Mason, D.C.; Davenport, I.J.; Neal, J.C.; Schumann, G.J.P.; Bates, P.D. Near real-time flood detection in urban and rural areas using high-resolution synthetic aperture radar images. *IEEE Trans. Geosci. Remote Sens.* **2012**, *50*, 3041–3052. [CrossRef]
9. Tsai, Y.-L.S.; Dietz, A.; Oppelt, N.; Kuenzer, C. Remote sensing of snow cover using spaceborne SAR: A review. *Remote Sens.* **2019**, *11*, 1456. [CrossRef]
10. Schlaffer, S.; Matgen, P.; Hollaus, M.; Wagner, W. Flood detection from multi-temporal SAR data using harmonic analysis and change detection. *Int. J. Appl. Earth Obs. Geoinf.* **2015**, *38*, 15–24. [CrossRef]
11. Bhatt, C.M.; Rao, G.S.; Jangam, S. Detection of urban flood inundation using RISAT-1 SAR images: A case study of Srinagar, Jammu and Kashmir (North India) floods of September 2014. *Model. Earth Syst. Environ.* **2019**, *6*, 429–438. [CrossRef]
12. Manavalan, R. SAR image analysis techniques for flood area mapping—Literature survey. *Earth Sci. Inform.* **2016**, *10*, 1–14. [CrossRef]

13. Chen, X.; Cui, Y.; Wen, C.; Zheng, M.; Gao, Y.; Li, J. Flood Mapping with SAR and Multi-Spectral Remote Sensing Images Based on Weighted Evidential Fusion. In Proceedings of the IGARSS 2020–2020 IEEE International Geoscience and Remote Sensing Symposium, Waikoloa, HI, USA, 26 September–2 October 2020; pp. 2519–2522. [CrossRef]
14. DeVries, B.; Huang, C.; Armston, J.; Huang, W.; Jones, J.W.; Lang, M.W. Rapid and robust monitoring of flood events using Sentinel-1 and Landsat data on the Google Earth Engine. *Remote Sens. Environ.* **2020**, *240*, 111664. [CrossRef]
15. Islam, T.; Meng, Q. An exploratory study of Sentinel-1 SAR for rapid urban flood mapping on Google Earth Engine. *Int. J. Appl. Earth Obs. Geoinf.* **2022**, *113*, 103002. [CrossRef]
16. Li, Y.; Martinis, S.; Plank, S.; Ludwig, R. An automatic change detection approach for rapid flood mapping in Sentinel-1 SAR data. *Int. J. Appl. Earth Obs. Geoinf.* **2018**, *73*, 123–135. [CrossRef]
17. Amitrano, D.; Di Martino, G.; Iodice, A.; Riccio, D.; Ruello, G. Unsupervised Rapid Flood Mapping Using Sentinel-1 GRD SAR Images. *IEEE Trans. Geosci. Remote Sens.* **2018**, *56*, 3290–3299. [CrossRef]
18. Amitrano, D.; Di Martino, G.; Di Simone, A.; Imperatore, P. Flood Detection with SAR: A Review of Techniques and Datasets. *Remote Sens.* **2024**, *16*, 656. [CrossRef]
19. Tsyganskaya, V.; Martinis, S.; Marzahn, P.; Ludwig, R. Detection of Temporary Flooded Vegetation Using Sentinel-1 Time Series Data. *Remote Sens.* **2018**, *10*, 1286. [CrossRef]
20. Scarpino, S.; Albano, R.; Cantisani, A.; Mancusi, L.; Sole, A.; Milillo, G. Multitemporal SAR Data and 2D Hydrodynamic Model Flood Scenario Dynamics Assessment. *ISPRS Int. J. Geo-Inf.* **2018**, *7*, 105. [CrossRef]
21. Ritushree, D.; Garg, S.; Dasgupta, A.; Martinis, S.; Selvakumaran, S.; Motagh, M. Improving SAR-based flood detection in arid regions using texture features. In Proceedings of the 2023 International Conference on Machine Intelligence for GeoAnalytics and Remote Sensing (MIGARS), Hyderabad, India, 27–29 January 2023; IEEE: Piscataway, NJ, USA, 2023. Available online: https://ieeexplore.ieee.org/abstract/document/10064526/ (accessed on 2 April 2024).
22. Huang, M.; Jin, S. Backscatter Characteristics Analysis for Flood Mapping Using Multi-Temporal Sentinel-1 Images. *Remote Sens.* **2022**, *14*, 3838. [CrossRef]
23. Uddin, K.; Matin, M.A.; Thapa, R.B. Rapid Flood Mapping Using Multi-temporal SAR Images: An Example from Bangladesh. In *Earth Observation Science and Applications for Risk Reduction and Enhanced Resilience in Hindu Kush Himalaya Region*; Bajracharya, B., Thapa, R.B., Matin, M.A., Eds.; Springer International Publishing: Cham, Germany, 2021; pp. 201–210. [CrossRef]
24. Hitouri, S.; Mohajane, M.; Lahsaini, M.; Ali, S.A.; Setargie, T.A.; Tripathi, G.; D'antonio, P.; Singh, S.K.; Varasano, A. Flood Susceptibility Mapping Using SAR Data and Machine Learning Algorithms in a Small Watershed in Northwestern Morocco. *Remote Sens.* **2024**, *16*, 858. [CrossRef]
25. Gebrehiwot, A.; Hashemi-Beni, L.; Thompson, G.; Kordjamshidi, P.; Langan, T.E. Deep Convolutional Neural Network for Flood Extent Mapping Using Unmanned Aerial Vehicles Data. *Sensors* **2019**, *19*, 1486. [CrossRef]
26. Lacava, T.; Filizzola, C.; Pergola, N.; Sannazzaro, F.; Tramutoli, V. Improving flood monitoring by the Robust AVHRR Technique (RAT) approach: The case of the April 2000 Hungary flood. *Int. J. Remote Sens.* **2010**, *31*, 2043–2062. [CrossRef]
27. Faruolo, M.; Coviello, I.; Lacava, T.; Pergola, N.; Tramutoli, V. A multi-sensor exportable approach for automatic flooded areas detection and monitoring by a composite satellite constellation. *IEEE Trans. Geosci. Remote Sens.* **2013**, *51*, 2136–2149. [CrossRef]
28. Lacava, T.; Ciancia, E.; Faruolo, M.; Pergola, N.; Satriano, V.; Tramutoli, V. On the Potential of RST-FLOOD on visible infrared imaging radiometer suite data for flooded areas detection. *Remote Sens.* **2019**, *11*, 598. [CrossRef]
29. Tramutoli, V. Robust AVHRR Techniques (RAT) for environmental monitoring: Theory and applications. In *Earth Surface Remote Sensing II*; SPIE: San Diego, CA, USA, 1998; pp. 101–113.
30. Nghia, B.P.Q.; Pal, I.; Chollacoop, N.; Mukhopadhyay, A. Applying Google earth engine for flood mapping and monitoring in the downstream provinces of Mekong river. *Prog. Disaster Sci.* **2022**, *14*, 100235. [CrossRef]
31. Tiwari, V.; Kumar, V.; Matin, M.A.; Thapa, A.; Ellenburg, W.L.; Gupta, N.; Thapa, S. Flood inundation mapping-Kerala 2018; Harnessing the power of SAR, automatic threshold detection method and Google Earth Engine. *PLoS ONE* **2020**, *15*, e0237324. [CrossRef] [PubMed]
32. Gorelick, N.; Hancher, M.; Dixon, M.; Ilyushchenko, S.; Thau, D.; Moore, R. Google Earth Engine: Planetary-scale geospatial analysis for everyone. *Remote Sens. Environ.* **2017**, *202*, 18–27. [CrossRef]
33. Kumar, L.; Mutanga, O. Google Earth Engine applications since inception: Usage, trends, and potential. *Remote Sens.* **2018**, *10*, 1509. [CrossRef]
34. Copernicus Emergency Management Service. Directorate Space, Security and Migration, European Commission Joint Research Centre (EC JRC). Available online: https://emergency.copernicus.eu/ (accessed on 2 April 2024).
35. Tholey, N.; Clandillon, S.; DE Fraipont, P. The contribution of spaceborne SAR and optical data in monitoring flood events: Examples in northern and southern France. *Hydrol. Process.* **1997**, *11*, 1409–1413. [CrossRef]
36. Kuenzer, C.; Guo, H.; Huth, J.; Leinenkugel, P.; Li, X.; Dech, S. Flood mapping and flood dynamics of the Mekong delta: ENVISAT-ASAR-WSM based time series analyses. *Remote Sens.* **2013**, *5*, 687–715. [CrossRef]
37. Torres, R.; Snoeij, P.; Geudtner, D.; Bibby, D.; Davidson, M.; Attema, E.; Potin, P.; Rommen, B.; Floury, N.; Brown, M.; et al. GMES Sentinel-1 mission. *Remote Sens. Environ.* **2012**, *120*, 9–24. [CrossRef]
38. Lv, S.; Meng, L.; Edwing, D.; Xue, S.; Geng, X.; Yan, X.-H. High-Performance Segmentation for Flood Mapping of HISEA-1 SAR Remote Sensing Images. *Remote Sens.* **2022**, *14*, 5504. [CrossRef]

39. Lehner, B.; Verdin, K.L.; Jarvis, A. *New Global Hydrograph Derived from Spaceborne Elevation Data*; USGS: Fairfax, VA, USA, 2008; Volume 89.
40. Pekel, J.-F.; Cottam, A.; Gorelick, N.; Belward, A.S. High-resolution mapping of global surface water and its long-term changes. *Nature* **2016**, *540*, 418–422. [CrossRef] [PubMed]
41. Yamazaki, D.; Ikeshima, D.; Sosa, J.; Bates, P.D.; Allen, G.H.; Pavelsky, T.M. MERIT Hydro: A High-Resolution Global Hydrography Map Based on Latest Topography Dataset. *Water Resour. Res.* **2019**, *55*, 5053–5073. [CrossRef]
42. Spencer, P.; Faulkner, D.; Perkins, I.; Lindsay, D.; Dixon, G.; Parkes, M.; Lowe, A.; Asadullah, A.; Hearn, K.; Gaffney, L.; et al. The floods of December 2015 in northern England: Description of the events and possible implications for flood hydrology in the UK. *Hydrol. Res.* **2017**, *49*, 568–596. [CrossRef]
43. Marsh, T.J.; Kirby, C.; Muchan, K.; Barker, L.; Henderson, E.; Hannaford, J. *The Winter Floods of 2015/2016 in the UK—A Review*; Centre for Ecology & Hydrology: Wallingford, UK, 2016; 37p, ISBN 978-1-906698-61-4. Available online: https://nora.nerc.ac.uk/id/eprint/515303/1/N515303CR.pdf (accessed on 2 April 2024).
44. Richard Davies, France and Italy Floods, October 2020. 2022. Available online: https://www.efas.eu/en/news/france-and-italy-floods-october-2020 (accessed on 2 April 2024).
45. Samuele, D.P.; Federica, G.; Filippo, S.; Enrico, B.-M. A simplified method for water depth mapping over crops during flood based on Copernicus and DTM open data. *Agric. Water Manag.* **2022**, *269*, 107642. [CrossRef]
46. APNews. Spanish City Braces for Flooding from Swollen Ebro River. 2021. Available online: https://apnews.com/article/floods-europe-environment-and-nature-spain-zaragoza-6d389c275662c8c4066c838370690de1 (accessed on 2 April 2024).
47. El Pais News. Zaragoza on Orange Alert after Ebro River Bursts Its Banks. 2015. Available online: https://english.elpais.com/elpais/2015/03/02/inenglish/1425294638_990925.html (accessed on 2 April 2024).
48. Carreño Conde, F.; De Mata Muñoz, M. Flood monitoring based on the study of Sentinel-1 SAR images: The Ebro River case study. *Water* **2019**, *11*, 2454. [CrossRef]
49. Richard Davies, Flooding affects Navarre Region, Spain, December 2021. Available online: https://www.efas.eu/en/news/flooding-affects-navarre-region-spain-december-2021 (accessed on 2 April 2024).
50. Tramutoli, V. Robust Satellite Techniques (RST) for natural and environmental hazards monitoring and mitigation: Theory and applications. In Proceedings of the 2007 International Workshop on the Analysis of Multi-temporal Remote Sensing Images, Leuven, Belgium, 18–20 July 2007. [CrossRef]
51. Cian, F.; Marconcini, M.; Ceccato, P.; Giupponi, C.J.N.H.; Sciences, E.S. Flood depth estimation by means of high-resolution SAR images and lidar data. *Nat. Hazards Earth Syst. Sci.* **2018**, *18*, 3063–3084. [CrossRef]
52. Lewis, A.; Lacey, J.; Mecklenburg, S.; Ross, J.; Siqueira, A.; Killough, B.; Szantoi, Z.; Tadono, T.; Rosenavist, A.; Goryl, P.; et al. CEOS analysis ready data for Land (CARD4L) overview. In Proceedings of the IGARSS 2018-2018 IEEE International Geoscience and Remote Sensing Symposium, Valencia, Spain, 22–27 July 2018; IEEE: Piscataway, NJ, USA, 2018; pp. 7407–7410. Available online: https://ieeexplore.ieee.org/abstract/document/8519255/ (accessed on 2 April 2024).
53. Lee, J.-S.; Grunes, M.; de Grandi, G. Polarimetric SAR speckle filtering and its implication for classification. *IEEE Trans. Geosci. Remote Sens.* **1999**, *37*, 2363–2373.
54. Lemoine, G. Refined Lee GEE Implementation. Available online: https://code.earthengine.google.com/5d1ed0a0f0417f098fdfd2fa137c3d0c (accessed on 2 April 2024).
55. Hoekman, D.H.; Reiche, J. Multi-model radiometric slope correction of SAR images of complex terrain using a two-stage semi-empirical approach. *Remote Sens. Environ.* **2015**, *156*, 1–10. [CrossRef]
56. Vollrath, A.; Mullissa, A.; Reiche, J. Angular-based radiometric slope correction for Sentinel-1 on Google Earth Engine. *Remote Sens.* **2020**, *12*, 1867. [CrossRef]
57. Mullissa, A.; Vollrath, A.; Odongo-Braun, C.; Slagter, B.; Balling, J.; Gou, Y.; Gorelick, N.; Reiche, J. Sentinel-1 SAR Backscatter Analysis Ready Data Preparation in Google Earth Engine. *Remote Sens.* **2021**, *13*, 1954. [CrossRef]
58. Farr, T.G.; Rosen, P.A.; Caro, E.; Crippen, R.; Duren, R.; Hensley, S.; Kobrick, M.; Paller, M.; Rodriguez, E.; Roth, L.; et al. The Shuttle Radar Topography Mission. *Rev. Geophys.* **2007**, *45*, RG2004. [CrossRef]
59. Tsyganskaya, V.; Martinis, S.; Marzahn, P. Flood Monitoring in Vegetated Areas Using Multitemporal Sentinel-1 Data: Impact of Time Series Features. *Water* **2019**, *11*, 1938. [CrossRef]
60. Copernicus Emergency Management Service. EMSR150: Flood in England. Available online: https://emergency.copernicus.eu/mapping/list-of-components/EMSR150 (accessed on 15 May 2024).
61. Copernicus Emergency Management Service. EMSR468: Flood in Piedmont Region, Italy. Available online: https://emergency.copernicus.eu/mapping/list-of-components/EMSR468/ALL/EMSR468_AOI01 (accessed on 15 May 2024).
62. Copernicus Emergency Management Service. EMSR118: Flood in Spain. Available online: https://emergency.copernicus.eu/mapping/list-of-components/EMSR118 (accessed on 15 May 2024).
63. Copernicus Emergency Management Service. EMSR279: Flood in the Ebro River Basin, Spain. Available online: https://emergency.copernicus.eu/mapping/list-of-components/EMSR279 (accessed on 15 May 2024).
64. Copernicus Emergency Management Service. EMSR555: Flood in the Ebro River Basin, Spain. Available online: https://emergency.copernicus.eu/mapping/list-of-components/EMSR555 (accessed on 15 May 2024).
65. Covello, F.; Battazza, F.; Coletta, A.; Lopinto, E.; Fiorentino, C.; Pietranera, L.; Valentini, G.; Zoffoli, S. COSMO-SkyMed an existing opportunity for observing the Earth. *J. Geodyn.* **2010**, *49*, 171–180. [CrossRef]

66. Yuan, C.; Wang, F.; Wang, S.; Zhou, Y. Accuracy evaluation of flood monitoring based on multiscale remote sensing for different landscapes. *Geomat. Nat. Hazards Risk* **2019**, *10*, 1389–1411. [CrossRef]
67. Nhangumbe, M.; Nascetti, A.; Ban, Y. Multi-Temporal Sentinel-1 SAR and Sentinel-2 MSI Data for Flood Mapping and Damage Assessment in Mozambique. *ISPRS Int. J. Geo-Inf.* **2023**, *12*, 53. [CrossRef]
68. Tegos, A.; Ziogas, A.; Bellos, V.; Tzimas, A. Forensic Hydrology: A Complete Reconstruction of an Extreme Flood Event in Data-Scarce Area. *Hydrology* **2022**, *9*, 93. [CrossRef]
69. Fohringer, J.; Dransch, D.; Kreibich, H.; Schröter, K. Social media as an information source for rapid flood inundation mapping. *Nat. Hazards Earth Syst. Sci.* **2015**, *15*, 2725–2738. [CrossRef]
70. Brouwer, T.; Eilander, D.; van Loenen, A.; Booij, M.J.; Wijnberg, K.M.; Verkade, J.S.; Wagemaker, J. Probabilistic flood extent estimates from social media flood observations. *Nat. Hazards Earth Syst. Sci.* **2017**, *17*, 735–747. [CrossRef]
71. Efstratiadis, A.; Dimas, P.; Pouliasis, G.; Tsoukalas, I.; Kossieris, P.; Bellos, V.; Sakki, G.-K.; Makropoulos, C.; Michas, S. Revisiting Flood Hazard Assessment Practices under a Hybrid Stochastic Simulation Framework. *Water* **2022**, *14*, 457. [CrossRef]
72. Lacava, T.; Papalia, L.B.; Paradiso, I.; Proto, M.; Pergola, N. The Cordinet Project: Analysis of the Barriers Limiting a More Diffuse and Systematic Use of Earth Observation Copernicus-Based Solutions. In Proceedings of the IGARSS 2020—2020 IEEE International Geoscience and Remote Sensing Symposium, Waikoloa, HI, USA, 26 September–2 October 2020; pp. 3166–3168. [CrossRef]
73. ESA. Sentinel-1B in-Flight Anomaly Summary Report. 2023. Available online: https://sentinel.esa.int/documents/247904/4819394/Sentinel-1B+In-Flight+Anomaly+Summary+Report.pdf (accessed on 2 April 2024).